Table 1. Chemical composition and characteristics of the precipitates prepared in this study

Sample	Phase	Annealing temperature	Theoretical composition[a]		Measured composition[a]		Color of precipitate	Lattice parameter[b]	
			Ca/(P + Nb)	Nb/(P + Nb)	Ca/(P + Nb)	Nb/(P + Nb)		*a*-axis (nm)	*c*-axis (nm)
NbHAp-0	HAp		1.60	0.000	1.60	–	White	–	–
NbHAp-I	HAp		1.60	0.017	1.56	0.013	Pale yellow	–	–
NbHAp-II	HAp		1.60	0.167	1.56	0.077	Buff yellow	–	–
NbTCPHAp-0	β-TCP + HAp	800°C	1.60	0.000	1.60	–	White	0.939	0.687
NbTCP/HAp-I	β-TCP + HAp	800°C	1.60	0.017	1.56	0.013	White	0.942	0.689
NbTCP/HAp-II	β-TCP + HAp	800°C	1.60	0.167	1.56	0.074	White	0.943	0.690

HAp, hydroxyapatite; NbHAp, hydroxyapatite containing Nb ions; TCP, tricalcium·phosphate
[a]Molar ratio
[b]Lattice parameter for HAp

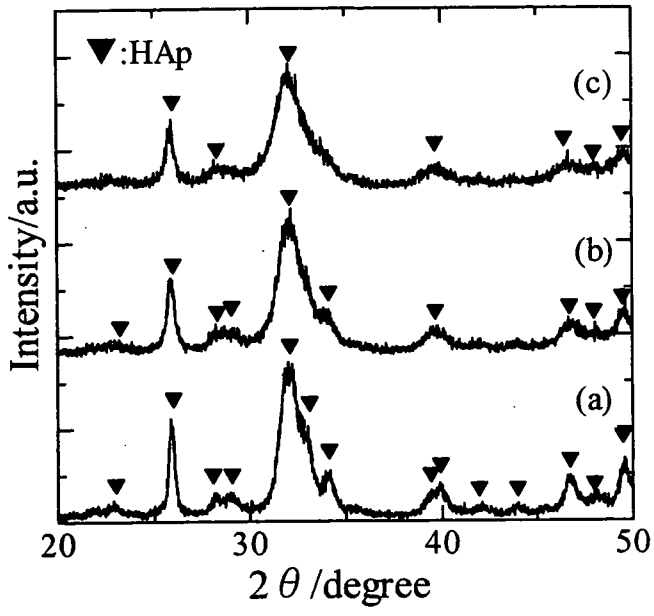

Fig. 1. X-ray diffraction (XRD) patterns of the precipitates with a Ca/(P + Nb) molar ratio of 1.50: *a*, Nb/(Nb + P) = 0; *b*, Nb/(Nb + P) = 0.0167; and *c*, Nb/(Nb + P) = 0.1667. *Triangles* represent XRD peaks due to the crystal structure of hydroxyapatite (HAp)

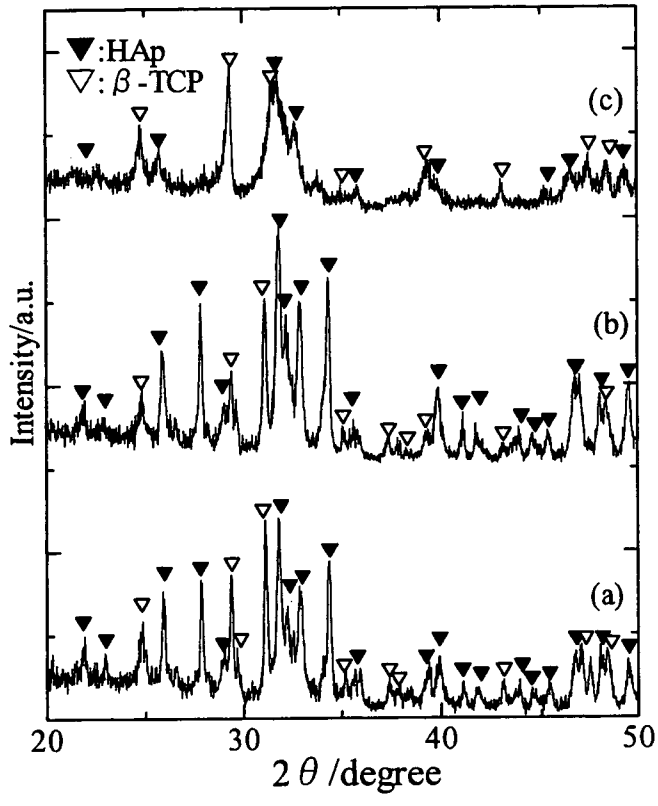

Fig. 2. XRD patterns of the annealed precipitates with a Ca/(P + Nb) molar ratio of 1.50: *a*, Nb/(Nb + P) = 0; *b*, Nb/(Nb + P) = 0.0167; and *c*, Nb/(Nb + P) = 0.1667. These precipitates were annealed at 800°C. *β-TCP*, β-tricalcium phosphate

their proliferation. All results were expressed as mean values ± SD and were analyzed statistically with Student's *t* test.

Results

XRD patterns of the precipitates prepared in this study are shown in Fig. 1. The XRD indicated that precipitates with Nb/(Nb + P) molar ratios from 0 to 0.167 had a monolithic apatite structure, irrespective of the Nb/(Nb + P) molar ratio of the starting solution, although the level of crystallite decreased as the Nb content increased. XRD patterns of the precipitates with various Nb/(Nb + P) molar ratios annealed at 800°C are shown in Fig. 2. The level of crystallites of the precipitates was high due to the annealing, and their diffraction peaks were composed of those of both HAp and β-TCP. Interestingly, the crystallite level decreased when the Nb level increased.

The chemical compositions and characteristics of the precipitates prepared in this study are summarized in Table 1. Both the Ca/(Nb + P) and the Nb/(P + Nb) molar ratios in precipitates measured by ICP approximately agreed with their theoretical values, except for the Nb/(P + Nb) molar ratio of NbTCP/HAp-II: the measured Nb/(P + Nb) molar ratio of NbTCP/HAp-II was 0.074, which is lower than the theoretical value of 0.167. The lattice parameter of the HAp phase in NbTCPHAp increased with increasing Nb content.

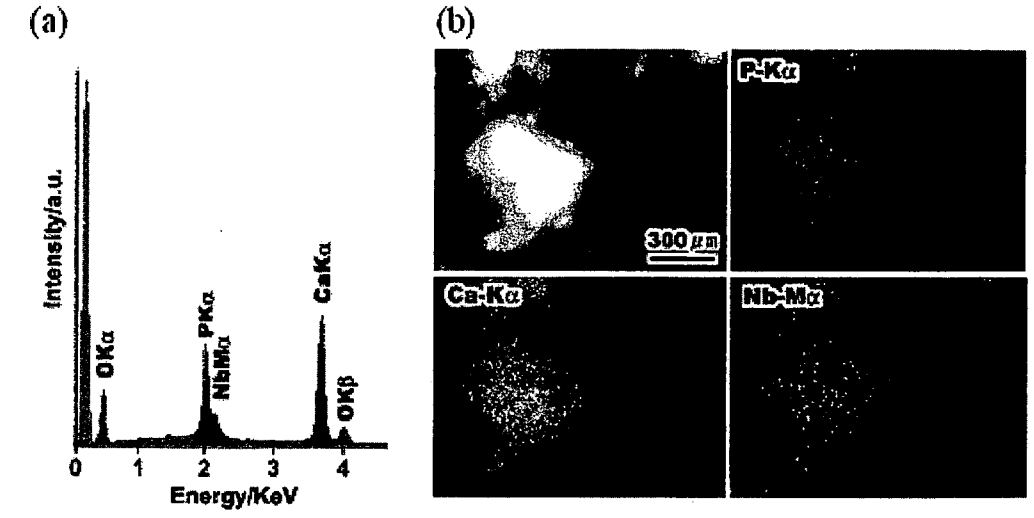

Fig. 3. Scanning electron microscopy–energy-dispersive X-ray spectroscopy spectra of NbTCP/HAp-II annealed at 800°C (**a**) and their mapping images from P-Kα, Ca-Kα, and Nb-Mα lines (**b**)

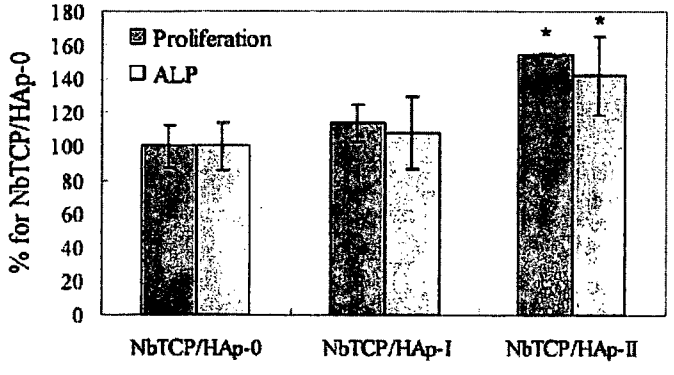

Fig. 4. Proliferation and alkaline phosphatase (*ALP*) activity of normal human osteoblasts (NHOst) cultured on various kinds of NbTCP/HAp pellets. *$P < 0.01$ against NbTCP/HAp-0 (without Nb ions)

The lattice parameters of NbTCP/HAp-0 without Nb ions were 0.939 nm for the *a*-axis and 0.687 nm for the *c*-axis, while those of NbTCP/HAp-II were 0.943 nm for the *a*-axis and 0.690 nm for the *c*-axis. In addition, the color of the precipitates became dark yellow as the Nb/(P + Nb) molar ratio increased, while the annealed precipitates of NbTCP/HAp were white.

SEM observation of the precipitates before annealing revealed that all precipitates were present as aggregates composed of primary particles of less than 1 μm in diameter, irrespective of the Nb/(P + Nb) molar ratio. Figure 3a shows SEM-EDX spectra of NbTCP/HAp-II. The EDX spectrum of Nb Mα was separated from the P K_α line and could be observed at 2.17 KeV, although its intensity was weak. The mapping images of the P-K_α, Ca-K_α, and Nb-M_α lines are shown in Fig. 3b. As shown in Fig. 3b, Nb ions were present at the same site as the Ca and P ions, suggesting that the Nb ions were homogenously distributed in the aggregates.

The proliferation and ALP activity of NHOst cultured on various kinds of NbTCP/HAp pellets is shown in Fig. 4. The proliferation of NHOst cultured on NbTCP/HAp-II pellets was approximately 60% higher than that on NbTCP/HAp-0 without Nb ions ($P < 0.01$). As shown in Fig. 5, many

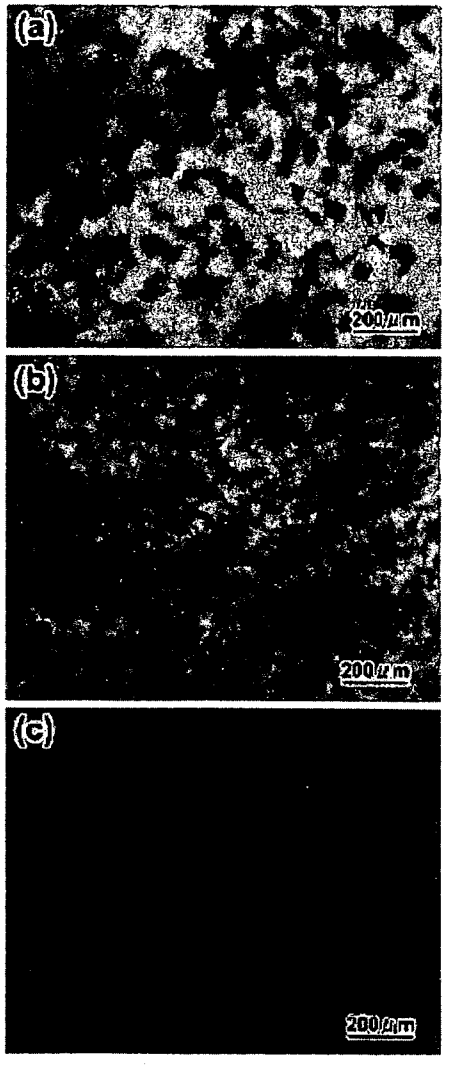

Fig. 5. Light microscopic images of NHOst cultured on various NbTCP/HAp samples for 7 days: *a*, NbTCP/HAp-0; *b*, NbTCP/HAp-I; and *c*, NbTCP/HAp-II. NHOst were stained by Giemsa solution

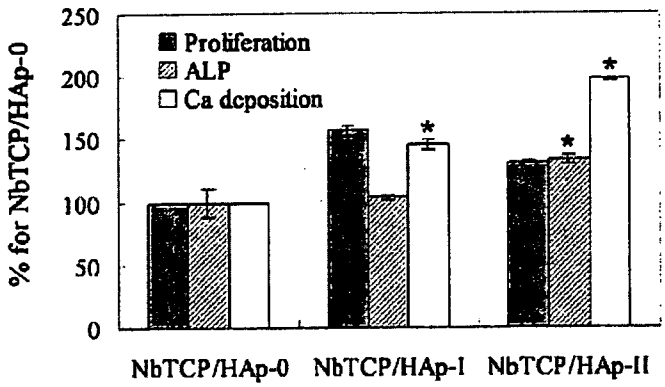

Fig. 6. Osteogenic properties (proliferation, ALP activity, and Ca deposition) of NHOst cultured in extracts from various NbTCP/HAp samples for 14 days. *$P < 0.01$ against NbTCP/HAp-0 (without Nb ions)

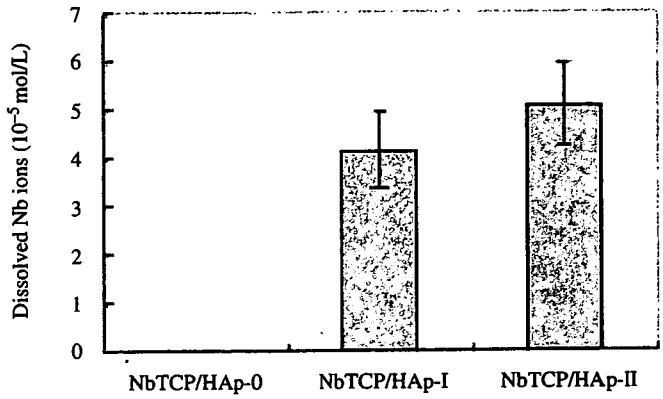

Fig. 7. Concentrations of Nb ions in extracts from various NbTCP/HAp samples. The concentration of Nb ions in cell culture medium was measured by inductively coupled plasma analysis

NHOst adhered to and spread on NbTCP/HAp-I and -II, while little spreading of NHOst was observed on HAp. In addition, as shown in Fig. 4, NHOst cultured on the NbTCP/HAp-II pellets expressed high ALP activity, compared with those cultured on NbTCP/HAp-0. Figure 6 shows the proliferation, ALP activity, and Ca deposition of NHOst cultured in extracts from various NbTCP/HAp samples for 14 days. Like the NHOst cultured on pellets, NHOst cultured in the extract from NbTCP/HAp-II expressed higher ALP activity than those in the extract from NbTCP/HAp-0. Furthermore, the amount of deposited calcium from NHOst increased with increasing Nb ion concentration in NbTCP/HAp, and the calcium deposition in the extract from NbTCP/HAp-II was twice that in the extract from NbTCP/HAp-0.

Figure 7 shows the concentration of Nb ions in extracts from NbTCP/HAp samples. It was found that Nb ions were released into the cell culture medium at concentrations of the order of 1×10^{-5} mol/l. To investigate the effect of Nb ions on NHOst function, NHOst were cultured in a medium containing Nb ions. The dependence of osteogenesis by NHOst on Nb ion concentration is shown in Fig. 8. Nb ions did not affect the proliferation of NHOst, but the ALP activity and Ca deposition of NHOst proceeded proportionally when the concentration of Nb ions was more than 1×10^{-5} mol/L.

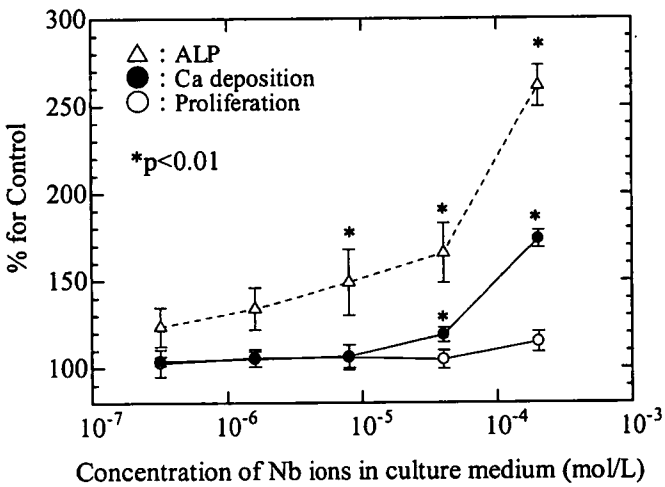

Fig. 8. Relationship between concentration of Nb ions in culture medium and osteogenic properties of NHOst. *$P < 0.01$ against cell culture medium without Nb ions

Discussion

Characterization of NbTCP/HAp biphasic calcium phosphate ceramics

As summarized in Table 1, before annealing the precipitates, the NbHAp samples were hydroxyapatite with low levels of crystallite. The hydroxyapatite structure is known to be very tolerant of ionic substitution.[12] Ca^{2+} ions, PO_4^{3-} ions, and OH^- ions can be replaced, partly or completely, by various cationic or anionic ions. Notably, as shown in Table 1, the lattice parameter of HAp increased when the Nb content in NbTCP/HAp was high. This fact suggests that Nb ions are taken into the apatite lattice. If a substitution of an Nb^{5+} ion for a Ca^{2+} ion in HAp occurred, the lattice parameter should decrease, since the ionic radius of Ca^{2+} and Nb^{5+} are 0.1 nm and 0.064 nm, respectively. Therefore, the possibility of substitution of Nb ions for Ca ions is low. On the other hand, although the structure of Nb ions in aqueous solution is not fully understood at present, it has been reported that Nb ions in solution are not present as Nb^{5+} but as niobiumate acid, $H_xNb_6O_{19}^{(8-x)-}$ ions (x = 0,1,2) for basic conditions,[14,15] and the niobiumate acid cluster ($H_xNb_6O_{19}^{(8-x)-}$) was polymerized or dissociated depending on the pH and ion concentration.[15] According to these reports, $H_4NbO_6^{3-}$ anionic monomer can exist in basal and low Nb concentrations (<0.08 M). Since the Nb concentration in this study was 0.01 M, Nb ions would exist as $H_4NbO_6^{3-}$ anionic monomers. $H_4NbO_6^{3-}$ may be substituted at the PO_4 site since the PO_4 site in HAp can be replaced by anionic

atomic groups. In addition, the ionic radius of the $H_4NbO_6^{3-}$ monomer and PO_4 are approximately 0.30 nm and 0.23 nm, respectively, suggesting that an increase in lattice parameter of NbTCP/HAp is ascribed to the substitution of PO_4 sites by this monomer in HAp. Furthermore, the fact that both the Ca/(Nb + P) and Nb/(P + Nb) molar ratios of the precipitates, as measured by ICP, approximately agreed with their theoretical values may support this hypothesis. Despite the theoretical Nb/(Nb + P) ratio being 0.1667, the Nb/(Nb + P) molar ratio in NbTCP/HAp-II was about 0.07, which suggests that the maximum amount of substituted Nb ions at the PO_4 site is around 0.07.

The Ca/(P + Nb) molar ratio in the NbHAp obtained in this study was lower than that of the stoichiometric value of 1.67 for HAp. Hydroxyapatite having a lower Ca/P molar ratio is known as calcium-deficient hydroxyapatite [Ca-def HAp, $Ca_{10-Z}(HPO_4)_Z(PO_4)_{6-Z}(OH)_{2-Z}$, Z = 0–1]. Therefore, NbHAp can be regarded as a Ca-def HAp in which the PO_4 sites are partly occupied by Nb ions.

Ca-def HAp decomposes to stoichiometric HAp and β-TCP at temperatures above 600°C according to the following reaction:[16,17]

$$Ca_{10-Z}(HPO_4)_Z(PO_4)_{6-Z}(OH)_{2-Z} \cdot nH_2O \rightarrow (1 - Z)Ca_{10}(PO_4)_6(OH)_2 + 3Z \cdot \beta\text{-}Ca_3(PO_4)_2 + Z \cdot nH_2O$$

The above thermal decomposition reaction occurred during the annealing of NbHAp, resulting in a lower Ca/P molar ratio than the stoichiometric value of HAp because of partial β-TCP formation. In addition, the homogenously distributed Nb ions in NbTCP/HAp may result from thermal diffusion of Nb ions during the thermal decomposition process.

Osteogenesis of NHOst cultured on NbTCP/HAp

In this study, NbTCP/HAp showed potential to promote calcification of NHOst. This study indicated that osteogenic behavior of NHOst cultured on NbTCP/HAp pellets was consistent with that of NHOst cultured in extracts from the pellets, suggesting that dissolved ions from the NbTCP/HAp pellets affect calcification of NHOst. As shown in Fig. 7, Nb ions were apparently released from NbTCP/HAps and dissolved in the medium at concentrations of the order of 1×10^{-5} mol/l. When 4×10^{-5} mol/l of $NbCl_5$ was added to the culture medium, Ca deposition clearly increased (Fig. 8). Therefore, the enhancement of Ca deposition is considered to be due to the dissolved Nb ions. One possible mechanism for enhancement of calcification is discussed below.

ALP is known to play an important role in the calcification of bone.[18–20] Generally, the calcification of bone mineral occurs in the matrix vesicles budding from the surface of osteoblasts.[21] The nucleation of biological apatite, which is the initial stage of calcification, occurs due to the reaction between inorganic PO_4^{3-} ions produced by the ALP and calcium ions in matrix vesicles.

NHOst cultured on the NbTCP/HAp pellets containing Nb ions expressed high ALP activity compared with those cultured on HAp without Nb ion. Similarly, it was found that NHOst cultured in an extract from NbTCP/HAp containing Nb ions expressed higher ALP activity than those in the extract from HAp without Nb ions. These results suggest that Nb ions affect the enhancement of ALP activity. Based on the above calcification mechanism in matrix vesicles, the enhancement of calcification might result from the enhancement of ALP activity due to dissolved Nb ions from NbTCP/HAp. The enhancement of ALP activity increases the production of inorganic PO_4^{3-} ions, and then the inorganic PO_4^{3-} ions produced may be taken into the matrix vesicles. The subsequent nucleation of biological hydroxyapatite occurs due to a reaction of Ca ions and inorganic PO_4^{3-} ions, followed by calcification. Although we cannot deny that Nb ions directly promote calcification by NHOst unrelated with ALP expression, the essence of the calcification enhancement by NbTCP/HAp may be the enhancement of ALP activity by Nb ions dissolved from NbTCP/HAp. The biological effect of Nb ions on NHOst is under investigation. Although further studies are necessary to clarify the mechanism of enhanced calcification by Nb ions, this study strongly suggests that NbTCP/HAp is a more promising material for use as a bone tissue engineering scaffold than HAp.

Conclusion

In order to promote the osteogenicity of osteoblasts, we synthesized a combination of HAp and β-TCP biphasic calcium phosphate containing Nb ions (NbTCP/HAp). The NbTCP/HAp samples were prepared by annealing precipitates obtained by coprecipitation of an aqueous solution of $Ca(NO_3)_2$ with a mixture of $(NH_4)_2HPO_4$ and aqueous Nb solution. The precipitates obtained by the coprecipitation process can be identified as Ca-def HAp, the PO_4 sites of which are partly occupied by Nb ions. NbTCP/HAp samples were successfully obtained by thermal decomposition of the precipitates.

NbTCP/HAp enhanced calcification of NHOst. The enhancement of calcification of NbTCP/HAp was ascribed to the enhancement of ALP activity due to the dissolved Nb ions from NbTCP/HAp.

Acknowledgments This study was supported in part by a Grant-in-Aid for Scientific Research on Advanced Medical Technology from the Ministry of Labour, Health and Welfare of Japan, and a Grant-in-Aid from the Japan Health Sciences Foundation.

References

1. Service FR. Tissue engineers build new bone. Science 2000;289: 1498–1500
2. Tamai N, Myoui A, Tomita T, Nakase T, Tanaka J, Ochi T, Yoshikawa H. Novel hydroxyapatite ceramics with an interconnective porous structure exhibit superior osteoconduction in vivo. J Biomed Mater Res 2002;59:110–117
3. Ohgushi H, Goldberg VM, Caplan IA. Heterotopic osteogenesis in porous ceramics induced by marrow cells. J Orthop Res 1989;7: 568–578

4. Cheung SH, Haak HM. Growth of osteoblasts on porous calcium phosphate ceramic: an in vitro model for biocompatibility study. Biomaterials 1989;10:63–67
5. Uchida A, Nade S, McCartney E, Ching W. Growth of bone marrow cells on porous ceramics in vitro. J Biomed Mater Res 1987;21: 1–10
6. Ohgushi H, Okumura M. Osteogenic capacity of rat and human marrow cells in porous ceramics. Acta Orthop Scand 1990;61: 431–434
7. Schopper C, Ziya-Ghazvini F, Goriwoda W, Moser D, Wanschitz F, Spassova E, Lagogiannis G, Auterith A, Ewers R. HA/TCP compounding of a porous CaP biomaterial improves bone formation and scaffold degradation – a long term histological study. J Biomed Mater Res B 2005;74B:458–467
8. Yuan H, Van DDM, Shihong L, Groot BV, Bruijn DDJ. A comparison of the osteoinductive potential of two calcium phosphate ceramics implanted intramuscularly in goats. J Mater Sci Mater Med 2002;13:1271–1275
9. Yamamoto A, Honma R, Sumita M. Cytotoxicity evaluation of 43 metal salts using murine fibroblast and osteoblastic cells. J Biomed Mater Res 1998;39:331–340
10. Isama K, Tsuchiya T. Bull Natl Inst Health Sci 2003;121:111
11. Tamai M, Nakaoka R, Isama K, Tsuchiya T. Novel calcium phosphate ceramics: the remarkable promoting action on the differentiation of normal human osteoblasts. Key Eng Mater 2006; 309–311:97–100
12. Ohya T, Ban T, Ohya Y, Takahashi Y. Preparation of concentrated, halogen-free aqueous titanium solution. Ceram Trans 2001;112: 47–52
13. Elliott CJ. Structure and chemistry of the apatites and other calcium orthophosphates. Tokyo: Elsevier, 1994
14. Cotton AF, Wilkinson G. Advanced inorganic chemistry. Tokyo: Baifukan, 1994
15. Jehng JM, Wachs IE. Niobium oxide solution chemistry. J Raman Spec 1991;22:83–89
16. Tamai M, Nakamura M, Isshiki T, Nishio K, Endoh H, Nakahira A. A metastable phase in thermal decomposition process of Ca-deficient hydroxyapatite. J Mater Sci Mater Med 2003;14: 617–622
17. Gibson IR, Rehman I, Best SM, Bonfield W. Characterization of the transformation from calcium-deficient apatite to beta-tricalcium phosphate. J Mater Sci Mater Med 2000;11:533–539
18. Genge RB, Sauer RG, Wu YLN, McLean MF, Wuthier ER. Correlation between loss of alkaline phosphatase activity and accumulation of calcium during matrix vesicle-mediated mineralization. J Biol Chem 1988;263:18513–18519
19. Sowa H, Kaji H, Yamaguchi T, Sugimoto T, Chihara K. Smad3 promotes alkaline phosphatase activity and mineralization of osteoblastic MC3T-E1 cells. J Bone Miner Res 2002;17: 1190–1199
20. Wennberg C, Hessle L, Lundberg P, Mauro S, Narisawa S, Lerner HU, Millan LJ. Functional characterization of osteoblasts and osteoclasts from alkaline phosphatase knockout mice. J Bone Miner Res 2000;15:1879–1888
21. Anderson CH. Molecular biology of matrix vesicles. Clin Orthop 1995;314:266–280

PS型人工膝関節の動作状態における応力状態の解析

九州大学　応用力学研究所基礎力学部門
東藤　貢

吉塚林病院
長嶺　隆二

九州大学大学院　総合理工学府物質理工学専攻
山口　勝太

日本臨床バイオメカニクス学会誌, Vol. 28, 2007.

PS型人工膝関節の動作状態における応力状態の解析

東藤　貢[※1]　長嶺　隆二[※2]　山口　勝太[※3]

Analysis of Stress States in PS Type Knee Prostheses under Dynamic Motion.

Mitsugu TODO, PhD., Ryuji NAGAMINE, MD., Shota YAMAGUCHI

Abstract

Using CAD data, 3-D finite element models of two kinds of PS-type knee prostheses, the first model and the second model, were constructed using a nonlinear spring model and analytical load data for deep squatting. The first model was previously used in TKA, and the second model is the most recent version with a modified design of the Post. Stress analysis was then performed by finite element analysis (FEA) under dynamic flexion motion from 0 to 135 degree. It was shown that only the condyle surfaces of the femoral component and the tibial insert contacted each other from 0 to 60 degrees of flexion for both models, and the stress concentration in the second model was a bit higher than that in the first model. The FEA results also exhibited that severe stress concentration was generated at the Post of the tibial UHMWPE insert due to the Post/Cam contact. This kind of stress concentration may result in the deformation and failure of the Post. It was shown that the design modification applied to the latter model effectively reduced the stress concentration of the Post.

Key words : Total knee arthroplasty, UHMWPE insert, deep flexion, finite element analysis.

※1　九州大学　応用力学研究所基礎力学部門
〒816-8580　福岡県春日市春日公園6-1
※2　吉塚林病院
〒812-0041　福岡県福岡市博多区吉塚7-6-29
※3　九州大学大学院　総合理工学府物質理工学専攻
〒816-8580　福岡県春日市春日公園6-1

日本臨床バイオメカニクス学会誌，Vol. 28，2007.

Corresponding Author : Mitsugu TODO, PhD.
Kyushu University, Research Institute for Applied Mechanics
6-1 Kasuga-koen, Kasuga City, 816-8580, Japan
Tel : 092-583-7762　　Fax : 092-583-7763
E-mail address : todo@riam.kyushu-u.ac.jp

緒　　言

重度の変形性膝関節症の患者に対しては，人工膝関節全置換術（total knee arthroplasty ; TKA）を行うことで患者のQOLが大幅に回復される．人工膝関節の高機能化のためにはTKAを施した膝関節の人体内での動作状態を詳細に把握し，設計へ反映させることが重要であるが，その動きは屈曲，内外旋，ロールバックなどの運動が複合的に生じており，完全には把握されていないのが現状である．そのため複合動作状態での過度の応力集中による脛骨インサートの疲労破壊や磨耗，またPost-Cam機構に特徴を持つPS型人工膝関節においては，脛骨インサートのPostの損傷などが重要な問題となっている．したがって，脛骨インサートにおける応力状態を知ることが重要であり，有限要素解析（finite element analysis ; FEA）による動作状態における応力解析が有用な知見を与えると考えられる．しかし，これまでに行われたTKAの3次元FEAのほとんどは歩行解析を対象としており[1),2)~5),8)]，一部深屈曲を考慮した解析は行われているものの[9)]，ある特定の屈曲角度に対して静的解析を行ったのみであり，連続的に立位から深屈曲までの動作を解析した例はほとんど行われていない．筆者らの研究グループは，これまでCADデータを用いた3次元FEAモデルの構築と，深屈曲や回旋を含む動作状態での応力解析について研究を進めてきた[10,11)]．なお，人工関節でみられるような高度の接触運動について陰解法FEAと陽解法FEAで解析し比較検討してきたが，陰解法では対応できないことが多く，陽解法の方が適応範囲が広いため，本解析でも陽解法汎用FEAコードのLS-DYNAを用いて屈曲解析を行った．

本研究では，旧型と新型の2種類のPS型人工膝関節のCADデータより3次元FEAモデルを構築し，非線形スプリングモデルおよびスクワットの荷重データを利用することで，立位から深屈曲までにいたる動作状態での脛骨インサートの応力状態を解析した．得られた結果を用いて，広範囲での屈曲が脛骨インサートの顆部およびPostの応力状態に及ぼす影響を詳細に調べ，旧型と新型を比較することで応力状態に及ぼすデザインの影響ならびに深屈曲への適応性について考察した．

有限要素解析モデルの構築

今回解析で用いた2種類のPS型人工膝関節は，過去に使用されていたモデル（1stモデル），および現在使用されているモデル（2ndモデル）である．2ndモデルは1stモデルの改良型とみなすことができ，特に脛骨インサートのPostならびに大腿骨コンポーネントのCamについて形状が変更されている．Postについては角部をなだらかにすることで丸みをもたせ，また，顆部とPostの境界部に溝を導入している．CamについてはPostと接触する面積をより大きくしており，これらの形状の変更により応力集中の低減を図っている．これら2機種のモデルのCADデータを基に，大腿骨コンポーネント，脛骨インサート，および脛骨コンポーネントから構成される3次元FEAモデルを構築した．ここで，大腿骨コンポーネントにおいて，脛骨インサートと接触する箇所（顆部）以外の微小な部分や，脛骨コンポーネントのステムなどは，解析結果にほとんど影響を与えないため，取り除いて簡略化を行った．簡略化した

モデルを図１に示す．FEA用プリプロセッサFEMAPを用いて要素分割を行ったモデルを図２に示す．用いた要素は４節点４面体要素であり，1stモデルの節点数は21,958，要素数は89,322，2ndモデルの節点数は28,254，要素数は121,604である．表１に解析で使用した材料定数を示す．本解析ではUHMWPE製の脛骨インサートは弾塑性体とし，図３に示すような３直線近似の応力—ひずみ曲線を採用した[7]．Co-Cr合金製の大腿骨コンポーネントとTi合金製の脛骨コンポーネントはUHMWPEに比べて100倍以上のヤング率を有しており，解析時間の節約のため剛体として解析を行った．また，大腿骨コンポーネント，脛骨インサート間の摩擦係数は0.04とし[5]，脛骨インサートと脛骨コンポーネント間は接合を仮定し，節点を共有させた．

人工膝関節の屈曲運動をFEAで再現すると，大腿骨コンポーネントと脛骨インサートの顆部間に摩擦力が生じる．PS型人工膝関節においては，屈曲が進むとPostとCamが接触し反力も生じるようになる．実際の人体膝では，関節の周囲に存在する軟部組織の張力とこれらの力がバランスし，たとえばロールバック等の動きが生じる．本研究で作成した簡易FEAモデルでこのような状況を再現するため，非線形バネモデルを導入した[8]．図４に示すように脛骨コンポーネントの前後に２本ずつ，合計４本の非線形バネ要素を取りつけた．このバネモデルにおいて力Fと変位dの関係は次式で示される．

$$F=0.18667d^2+1.3313d \quad \cdots\cdots (1)$$

なお，この非線形構成則は十字靭帯を切除した場合の膝の状態を想定したものである[8]．

通常TKA膝の屈曲には内旋が同時に生じることが多く，たとえば，135degの屈曲では７deg程度の内旋が生じることが報告されているが[12]，本研究では，まずPost部への影響がより高く，またその影響を明確にするため屈曲運動のみを考慮して境界条件を設定した．屈曲方法としては大腿骨コンポーネントの顆部表面の曲面に沿った円の中心を通る軸を設定し回転軸とした．屈曲時の角速度については，予備解析として，１deg/msと0.1deg/msの２種類について比較検討したが，１回の解析に前者で約10時間，後者で約100時間を要し，また応力状態については差は殆どなかったため，計算効率を考慮して１deg/msを選択

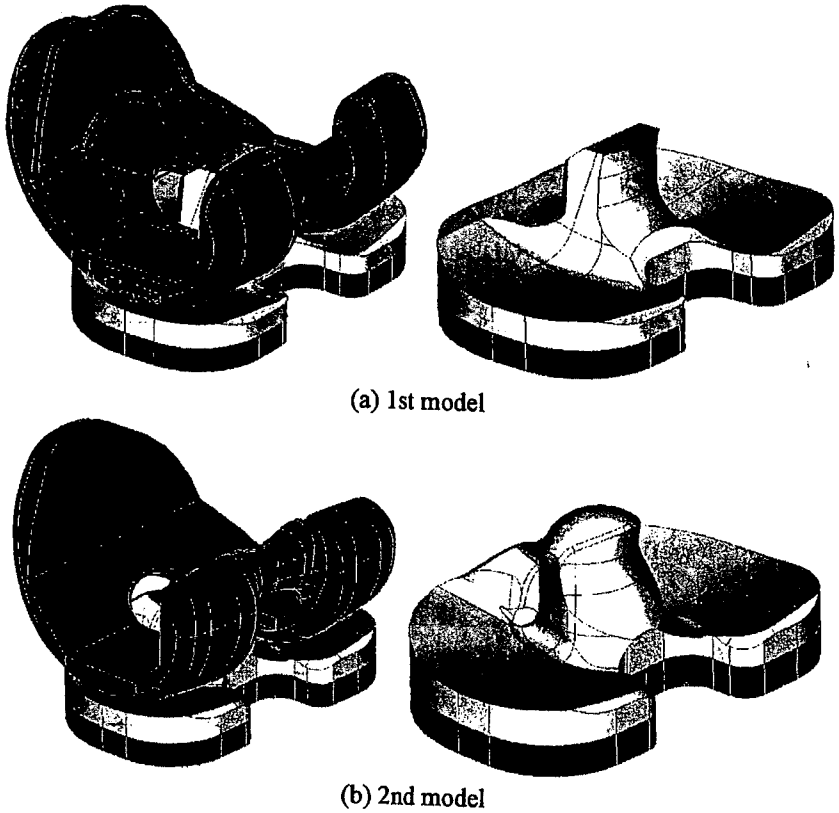

(a) 1st model

(b) 2nd model

図１．FEA models of two kinds of PS type knee prostheses.
(a) 1st model (b) 2nd model

表１．Material constants for FEA.

Parts	Material	Density (kg/m^3)	E (MPa)	ν	σ_Y (MPa)
Tibial insert	UHMWPE	940	880	0.4	16

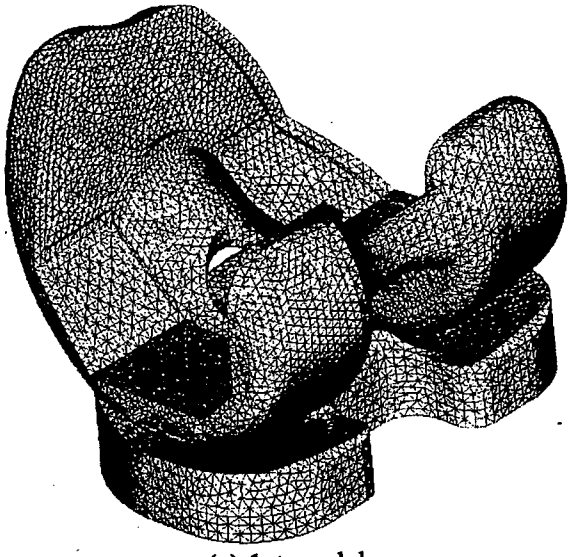

(a) 1st model

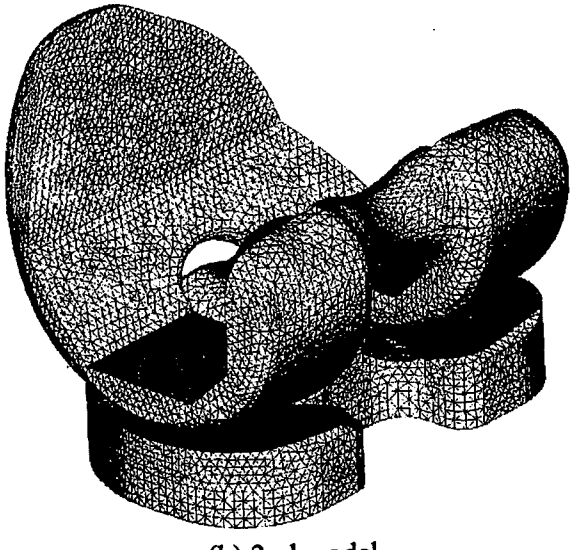

(b) 2nd model

図2. FEA mesh models of PS type knee prostheses.
(a) 1st model (b) 2nd model

した．荷重に関しては，健常膝がスクワットを行う場合について，筋力を考慮した2次元モデルから求められた解析的荷重データを参考にした[2]．大腿骨コンポーネントには荷重P_1を鉛直方向（Z方向）に，また，脛骨コンポーネントには荷重P_2を水平方向（Y方向）に加えた．これらの荷重値を屈曲角度の関数として図5に示す．なお，拘束条件については，大腿骨コンポーネントはZ方向以外の変位を固定し，脛骨コンポーネントはY方向以外の変位を固定し

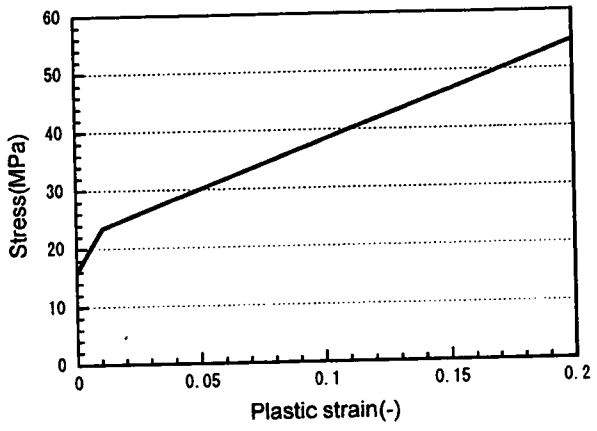

図3. Bi-linear relation of stress-plastic strain curve of UHMWPE.

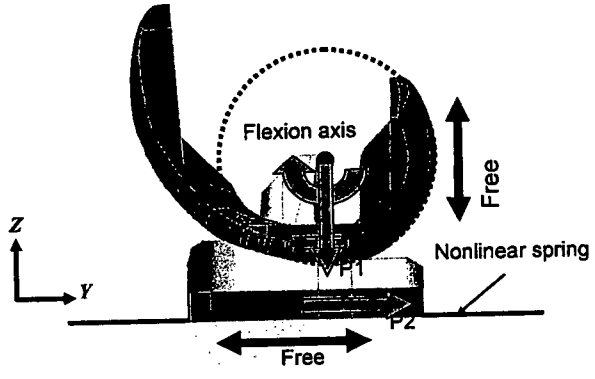

図4. Boundary conditions of the TKA model.

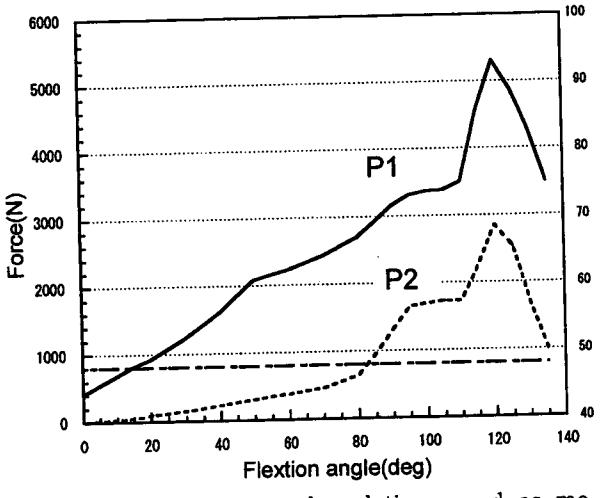

図5. Force-flexion angle relations used as mechanical boundary condition.

た．なお，応力解析に用いた陽解法汎用FEAコードはLS-DYNAである．

結　　果

図6に応力解析から得られた45degと120deg

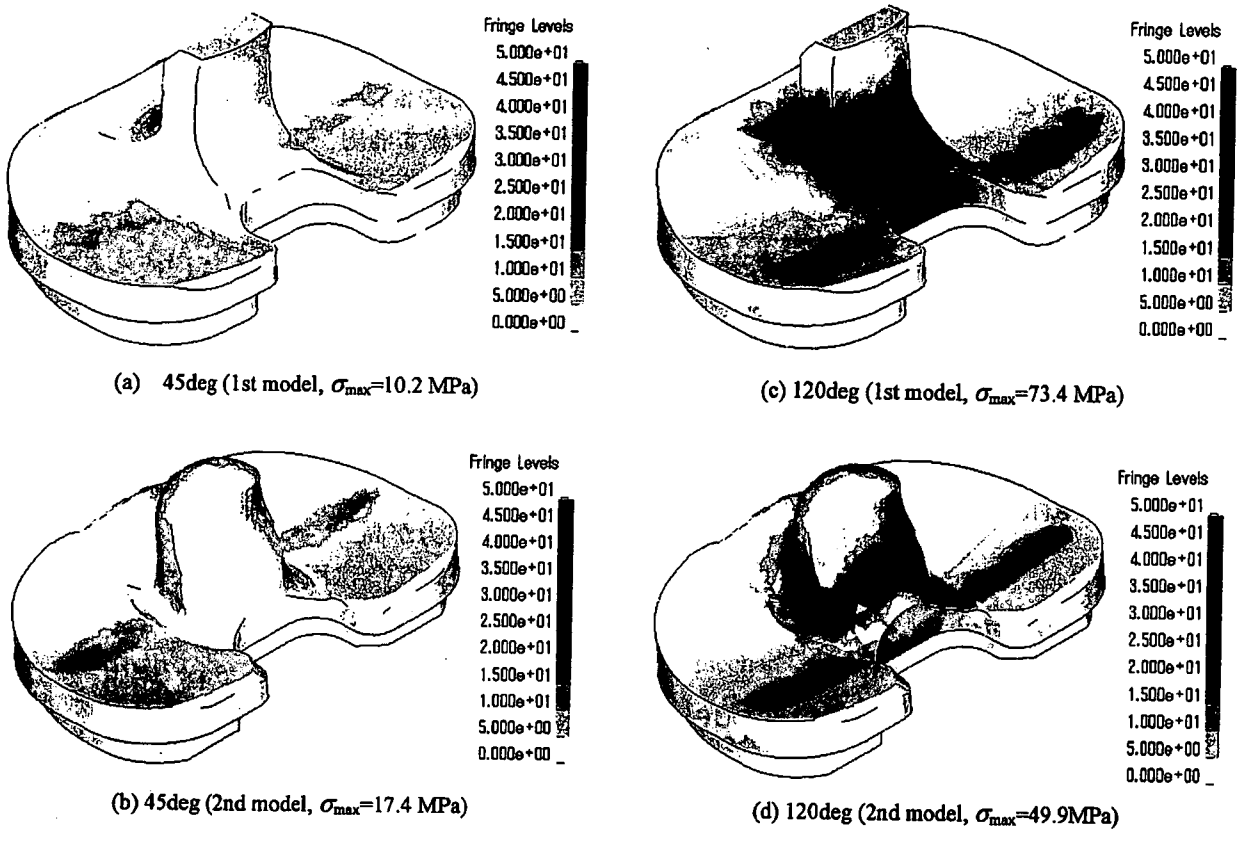

(a) 45deg (1st model, σ_{max}=10.2 MPa)

(c) 120deg (1st model, σ_{max}=73.4 MPa)

(b) 45deg (2nd model, σ_{max}=17.4 MPa)

(d) 120deg (2nd model, σ_{max}=49.9MPa)

図6. Equivalent stress distribution on the surface of tibial insert (unit : MPa).
(a) 45deg (1st model, σ_{max} = 10.2 MPa)
(b) 45deg (2nd model, σ_{max} = 17.4 MPa)
(c) 120deg (1st model, σ_{max} = 73.4 MPa)
(d) 120deg (2nd model, σ_{max} = 49.9MPa)

でのミーゼス相当応力分布図を示す. 45degの屈曲状態では応力集中は顆部表面のみで生じており, 1stモデルでの最大応力値は10.2MPa, 2ndモデルでは17.4MPaであった. この角度ではまだPost-Camの接触は生じていなかった. 120degの屈曲状態では, 顆部表面に加えPost部分でも大きな応力集中が生じていることがわかった. 最大応力値は1stモデルでは73.4MPa, 2ndモデルでは49.9MPaとなっており, 1stモデルでは2ndモデルの1.5倍程度の応力集中が生じていた. また, 顆部表面の応力集中部は45degに比べると後方 (Y方向) に移動しており, ロールバックが生じていることが分かった. 図7にバネモデルの変位量の屈曲角度依存性を示す (図4で−Y方向が正). 屈曲角度が60deg付近までは変位はほとんど生じていな

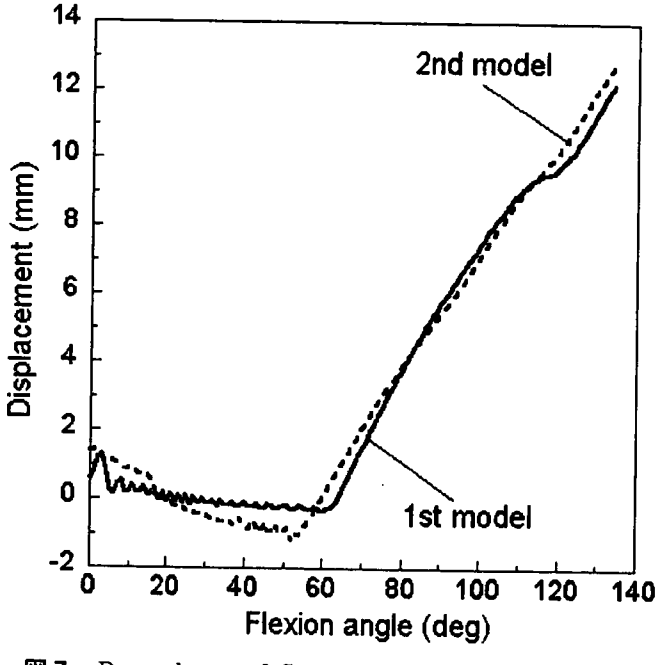

図7. Dependence of flexion angle on displacement of spring model.

いが，60deg以降は急激に増加し，最終的に12mm程度の変位が生じている．なお，2機種の間での差は殆どみられない．この60deg以降でみられるバネモデルの変位，すなわち脛骨コンポーネントの－Y方向への移動がロールバックに対応する．

図8に脛骨インサート顆部とPost部での最大相当応力の推移を示す．顆部での応力（図-(a)）を比較すると，60deg以下では2ndモデルの方が1stモデルより大きく，120deg以上になると1stモデルの方が大きな応力を示すが，後述のPost部に比べると全体的にその差は小さかった．2ndモデルの脛骨コンポーネントの前顆部の傾斜は，1stモデルよりも若干緩やかであり，そのため60deg以下では，大腿骨顆部との接触がより点接触に近くなり応力が高くなったと考えられる．後顆部の傾斜は両機種でほとんど同じであるため応力の差も小さかった．次にPost部での応力（図-(b)）を比較すると，Post-Camの接触が1stモデルでは64degから始まっているのに対して，2ndモデルでは54degから始まっていることが分かった．この差は2ndモデルのPost形状が1stモデルに比べて太くなっているためであると推測される．100degまでは2ndモデルの方が1stモデルより高い応力を示すが，100deg以上では，1stモデルにおける応力集中が急激に増加し大小関係は逆転した．1stモデルは2ndモデルに比べてPost/ Camの接触面積が小さいためこのような急激な応力集中が起きていることが予想される．なお，図-(a)において応力値が変動しているが，これはバネ要素を取り付けた頸骨コンポーネントの振動，頸骨インサート中の応力波の反射などの動的効果の影響によるものと考えられる．

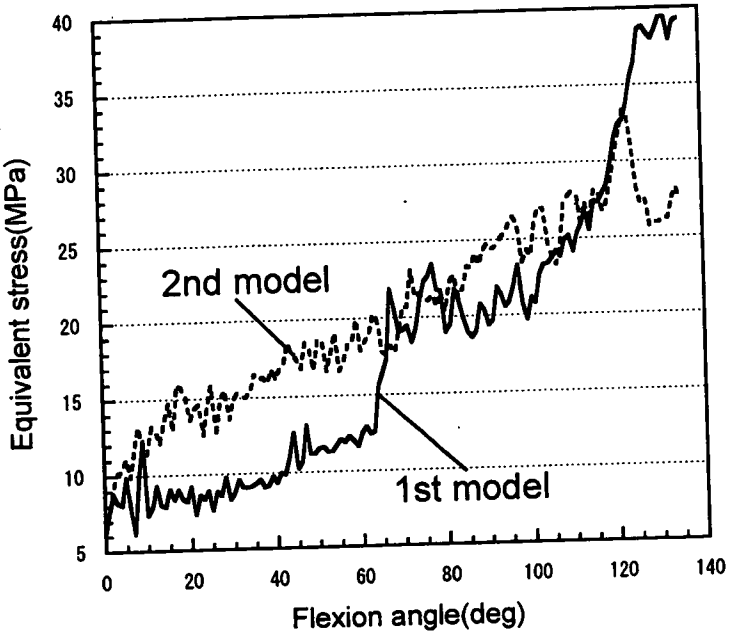

(a) condyle surface

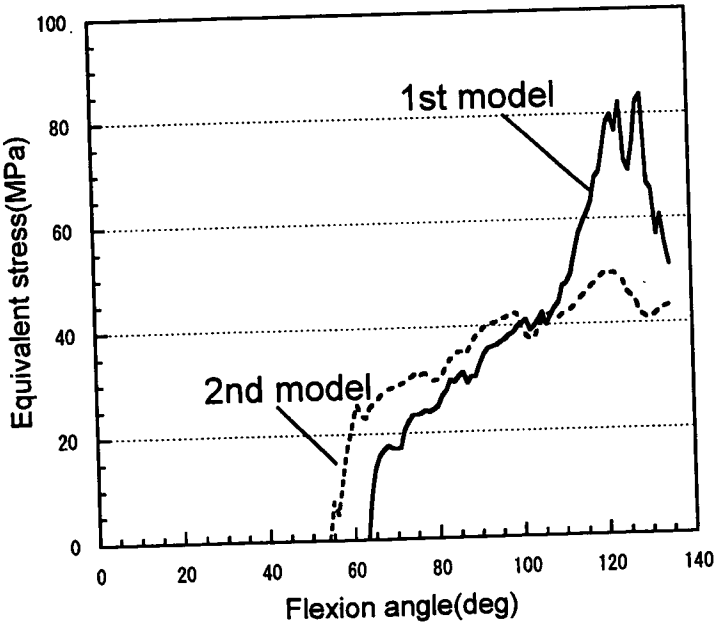

(b) post surface

図8．Maximum equivalent stress history on the surface of tibial insert.
(a) condyle surface
(b) Post surface

考　　察

以上の解析結果より，1stモデルから2ndモデルに移行する際に考慮されたデザインは，Post部の応力集中を効果的に減じていることがわかった．このような応力集中の軽減は，深屈曲時

にPostとCamの接触により生じる抵抗力（Postの接触面に作用する応力の総和として表される反力）が低くなることに対応しており，このような抵抗力の低下は屈曲に対する抵抗の軽減を意味しているため，2ndモデルは1stモデルに比べより深屈曲を容易にする人工膝関節であると考えられる．なお，屈曲角が100deg以下では1stモデルの方が応力集中の状態が低くかったことから，低屈曲では1stモデルのデザインの方が2ndモデルよりも脛骨インサートの磨耗に対してはより効果的であると考えられる．

結　　言

2種類のPS型人工膝関節のCADデータから3次元FEAモデルを構築し，135degまでの広範囲の屈曲状態での応力解析を行った．得られた結果は以下の通りである．

(1)大腿骨・脛骨コンポーネント，脛骨インサート，および非線形バネモデルからなる簡易モデルに，スクワット解析から得られた荷重データを利用することで，広範囲の屈曲状態での応力解析を可能とする3次元FEAモデルを考案した．

(2)深屈曲時においてPost/Camの接触によりPost部に高い応力集中が生じていることが確認できた．また，非線形バネモデルの導入によりロールバックを再現することができた．

(3)2ndモデルで採用されたPost部のデザイン変更は，効果的に深屈曲での応力集中を軽減しており，このことはPost/Cam接触により生じる抵抗力の低減に対応しているため，2ndモデルは1stモデルに比べてより深屈曲を容易にする人工膝関節であると考えられる．

文　　献

1）Ahir SP, Blunn GW et al. : Evaluation of a testing method for the fatigue performance of total knee tibial trays. J Biomech 32 : 1049-1057, 1999.

2）Dahlkvis NJ, Mayo P, Seedhom BB : Forces during squatting and rising from a deep squat. Eng Med 11 : 69-76. 1982.

3）Darryl D, D'Lima MD et al. : Impact of patellofemoral design on patellofemoral forces and polyethylene stresses. J Bone Joint Surg 85A: 85-93, 2003.

4）Godest AC, Beaugonin M et al. : Simulation of a knee joint replacement during a gait cycle using explicit finite element analysis. J Biomech 35 : 267-275, 2002.

5）Halloran JP, Anthony JP et al. : Explicit finite element modeling of total knee replacement mechanics. J Biomech 38 : 323-331, 2005.

6）金粕浩一：TKAの機種と可動域—Scopio Superflex PSの臨床成績と可動域及び動態解析—．関節外科 23 : 49-57, 2004.

7）小林公一，柿木俊彦 他：超高分子量ポリエチレンの衝撃圧縮特性，実験力学，3（4）: 225-229, 2003.

8）Sathasivam S, Walker PS : Computer model to predict subsurface damage in tibial inserts of total knees. J Ortho Res 16 : 564-571, 1998.

9）Morra EA, Greenwald AS : Polymer insert stress in total knee designs during high-flexion activities: a finite element study. J Bone Joint Surg Am 87 : 120-124, 2005.

10）東藤貢，長嶺隆二 他：人工膝関節の3次元有限要素モデルの構築と計算効率に関する研究，日本臨床バイオメカニクス学会誌，27 : 231-237, 2006.

11）東藤貢，長嶺隆二 他：人工膝関節のUHMWPEインサートの応力状態に及ぼす屈曲と回旋の影響，日本臨床バイオメカニクス学会誌，27 : 239-246, 2006.

12）Watanabe T, Yamazaki T et al. : In vivo kinematics of mobile-bearing knee arthroplasty in deep knee bending motion. J Ortho Res 22 : 1044-1049, 2004.

Neurological Research
accepted.

Subtracted Vortex Centers Path Line Method with Cinematic Angiography for Measurement of Flow Speed in Cerebral Aneurysms

Makoto Ohta[1,2], Naoko Fujimura[1,3], Luca Augsburger[1], Krisztina Barath[1], Hasan Yilmaz[1], German Abdo[1], Karl-Olof Lovblad[1], Daniel A. Rüfenachat[1]

Neuroradiology, Geneva University Hospital

Biofluid Control laboratory, Institute of Fluid Science, Tohoku University

Abstract :

Background and Purpose: The assessment of blood flow speed by imaging modalities is of increasing importance for endovascular treatment, such as stent implantation, of cerebral aneurysms. The subtracted vortex centers path line method (SVC method) utilizes image post-processing for determining flow quantitatively. In current practice, intraaneurysmal flow in an in-vitro model is visualized by laser sheet translumination and digitally recorded. In this study, we applied this method to cinematic angiography (CA), which is the preferred imaging method for endovascular interventions, to analyze hemodynamic

changes. The SVC method was applied to the images and compared with results of the slipstream line method with colored fluid.

Methods: A transparent tubular model was constructed of silicone which included an aneurysm 10 mm in diameter and having a 5 mm neck on a straight parent artery with a diameter of 3.5 mm. The model was integrated into a pulsatile circulation system. By CA, successive images at 25 frames per second with injection of contrast were obtained.

Results and conclusion: Rotating vortexes of contrast, which advanced along the wall of the aneurysm, were observed in successive images of the aneurysm cavity. This phenomenon was also observed in the successive images with the slipstream line method. The speed of the vortex center was calculated and the results show that the vortex speed of CA was the same as that under the slipstream line method. This indicates the possibility of applying the SVC method to medical imaging equipment for analysis of the flow in aneurysms containing stent.

Introduction

With the availability of flexible stent placement for intracranial aneurysms, this relatively new treatment is recently being increasingly utilized (1-4). By decreasing the inflow into the aneurysm, stent treatment may lead to thrombus formation in intracranial aneurysms (5-10). The stent design, e.g., the design of the stent edge, critically impact on flow changes (11, 12).

The assessment of blood flow by imaging modalities is of increasing importance. Magnetic Resonance (MR), Computed Tomography (CT), or Digital Subtraction Angiography (DSA) are the three major techniques currently being applied for this purpose.

Wakhloo et al. used Ethiodol droplets for measurement of flow in arteriovenous malformations (AVM) (14). Isoda et al., for example, have investigated time-of-flight MR angiography in aneurysm models which enables the three-dimensional measurements (13). To evaluate intraaneurysmal hemodynamics using images acquired by DSA, Sadasivan et al. (15) and Asakura et al. (16) utilized time-density curves, and Sadasivan described the convection and diffusion components of flow and quantified the changes in flow in cerebral aneurysms after stents implantation.

The subtracted vortex centers path line (SVC) method was developed by Cassot and Barath, where an in vitro pulsatile circulation loop was seeded with particles and illuminated by a laser-sheet for measuring flow speed in a side-wall aneurysm model (17). In this SVC method, post-processing of successive images is employed to trace a rotating vortex of particles from which the speed of the vortex movement in the aneurysm can be determined. This vortex speed represents intraaneurysmal flow speed, which is a parameter that can be used for evaluating medical devices such as stents (18). Although this processing is very simple and easily employed in the clinical field, it has only been used with in-vitro setups, but never under in vivo conditions or by clinicians.

In this study, the SVC method was applied to successive contrast images acquired with cinematic angiography (CA). The distance which a vortex moved was compared with a slipstream line acquired by video to validate and confirm the feasibility of integrating this method in medical imaging devices.

Materials and methods

In-vitro model:

A transparent tubular model made of silicone (ELASTRAT Sarl., Geneva, Switzerland) including an aneurysm with a 5 mm neck and a diameter of 10 mm, which was situated on a straight parent artery 3.5 mm in diameter (Figure 1), was integrated into a circulation system. This model was based on the previous paper (17) to compare to the results. The pressure and the pulsatility (143/77 mmHg and 1 Hz, respectively) were measured at the injection point in the system (the flow rate was 200 ml / min). Water was used as fluid at room temperature. For varying the flow pattern in the aneurysm, a stent (Leo stent, 4 mm diameter, 1.5 cm long, BALT) was prepared and the flow speeds before and after its placement were measured.

Image acquisition:

CA

The image acquisition rate of CA (3D-RA, BV 3000, Philips Medical Systems

(PMS), The Netherlands) was 25 frames per second using imaging parameters of 60 kV and 300 mA. Each successive image was 512×512 bits in a 18.415 cm square with a 256 grayscale.

Slipstream line method

To compare images based on contrast with CA, a slipstream line was obtained by a video camera. Red hydrophilic liquid was introduced into the same circulation. The rate of the camera (DSC-T1, SONY, Japan) was 30 frames per second.

Post-processing

The SVC method was applied to the flow images of CA and the slipstream line, respectively, to quantify the flows.

All procedures of this processing were performed with commercially available based software packages which can be easily accessed by clinicians. Microsoft Photo Editor 3.01 (Microsoft Corporation, USA) was used for enhancement of image and subtraction was performed on JASC Paint Shop Pro 6.00 (Jasc Software, USA). Tracing the vortex center was carried out with NIH images